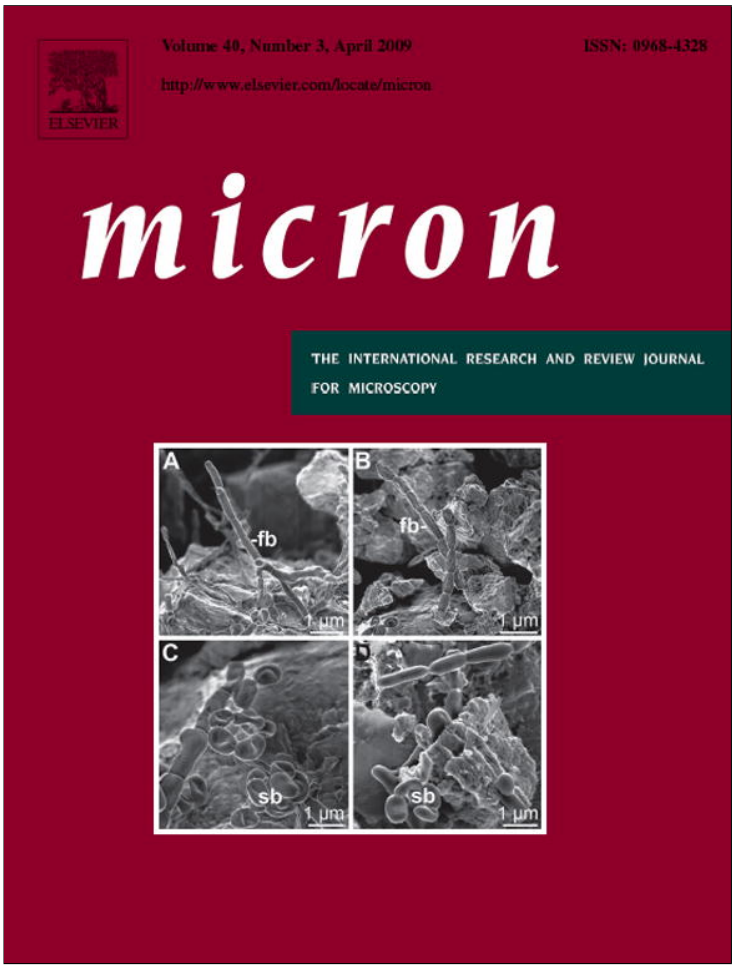

Micron 40 (2009) 335–342

Contents lists available at ScienceDirect

Micron

journal homepage: www.elsevier.com/locate/micron

Structures of planar defects in ZnO nanobelts and nanowires

Yong Ding, Zhong Lin Wang *

School of Materials Science and Engineering, Georgia Institute of Technology, Atlanta, GA 30332-0245, United States

ARTICLE INFO

Article history:
Received 21 September 2008
Received in revised form 23 October 2008
Accepted 24 October 2008

Keywords:
TEM
HRTEM
ZnO
Nanobelt
Nanowire
Planar defect
Stacking fault
Twin
Inversion domain wall

ABSTRACT

Quasi-one-dimensional (1D) nanostructures, such as nanowires, nanobelts and nanorods, are the forefront materials for nanotechnology. To date, such nanostructures have been synthesized for a wide range of semiconductors and oxides, and they are potential building blocks for fabricating numerous nano-scale devices. 1D ZnO nanostructures, due to its unique semiconducting, piezoelectric, and bio-safe properties, have received wide attention. From structure point of view, a common characteristic of ZnO nanostructures is that they are mostly dislocation-free. However, planar and point defects do frequently exist in such nanostructures. The objective of this paper is to present detailed electron microscopy study about the structures of planar defects, such as stacking faults, twins, inversion domain walls that existed in 1D ZnO nanostructures. These planar defects are important for understanding the growth mechanism and relevant physical and possibly chemical properties of 1D ZnO nanostructures.

1. Introduction

Since the discovery of semiconducting nanobelts in 2001 (Pan et al., 2001), research in one-dimensional (1D) nanostructures of functional oxide materials has attracted great attention due to their unique and novel applications in optics, optoelectronics, catalysis and piezoelectricity. Semiconducting nanobelts are a unique group of quasi-one-dimensional nanomaterials, which have been systematically studied for a wide range of materials with distinct chemical composition and crystallographic structures (Wang, 2003a,b). ZnO is such a key technological material. The lack of a center of symmetry in wurtzite-structured ZnO unit cell, combined with large electromechanical coupling, results in ZnO bulk, thin films and nanostructures strong piezoelectric and pyroelectric properties. In addition, ZnO is a wide band-gap (3.37 eV) compound semiconductor that is suitable for short wavelength optoelectronic applications. The high exciton binding energy (60 meV) in ZnO crystal can ensure efficient excitonic emission at room temperature and room temperature ultraviolet (UV) luminescence has been reported in disordered nanoparticles and thin films. Further, ZnO is transparent to visible light and can be made highly conductive by doping. To date, nanodevices, such as field effect transistors (Arnold et al., 2003), ultrasensitive nano-size gas sensors (Comini et al., 2002), nanoresonators (Bai et al., 2003) and nanocantilevers (Hughes and Wang, 2003), have been fabricated based on 1D ZnO nanobelts. Thermal transport along a single ZnO nanobelt has been measured (Shi et al., 2004). Very recently, ZnO nanobelts, nanosprings (Kong and Wang, 2003) and nanorings (Kong et al., 2004) that exhibit piezoelectric properties have been synthesized, which could be a candidate for nano-scale traducers, resonators and sensors.

In most cases, dislocations cannot be pinned in the volume of 1D nanostructures, and they can easily migrate to the surfaces and finally disappear. As a result, most of the 1D nanostructures are dislocation-free. The only chance we observed a few dislocations is in heavily distorted ZnO fine nanowires, whose diameter is only around 6 nm (Ding and Wang, 2004). The most common defects in 1D ZnO nanostructures are planar defects, such as twins, stacking faults, and inversion domain walls, et al. These defects are not only essential for the growth of the nanostructures, but also strongly affect their optical, electrical and possibly chemical properties. The purpose of this paper is to systematically study the planar defects present in 1D ZnO nanostructures using high-resolution transmission electron microscopy (HRTEM). Our objective is to reveal the atomic-scale structure of planar defects. Discussions will be presented about the role played by planar defects in the formation and growth of 1D ZnO nanostructures.

* Corresponding author.
E-mail address: zhong.wang@mse.gatech.edu (Z.L. Wang).

0968-4328/$ – see front matter © 2008 Elsevier Ltd. All rights reserved.
doi:10.1016/j.micron.2008.10.008

2. Experiments

The detailed synthesis processes of 1D ZnO nanostructures were described in related references (Ding and Wang, 2004; Kong et al., 2004). Transmission electron microscopy (TEM) study was carried out at 400 kV using JEM 4000EX. The software used to do the high-resolution TEM (HRTEM) simulation is Cerius2.

3. Results and discussion

3.1. Twins

From literature, twin structure is most common in face-centered cubic structured metallic nanoparticles and silicon based nanowires (Wiley et al., 2006; Sauer et al., 2002). For wurtzite structures, from theoretical point of view, the predicted possible twin boundaries are $(0\,1\,\bar{1}\,1)$, $(0\,1\,\bar{1}\,2)$ and $(0\,1\,\bar{1}\,3)$ (Bere and Serra, 2003). Theoretical calculations revealed that the $(0\,1\,\bar{1}\,3)$ twin has a relatively low energy. However, such twin boundary has not been observed in bulk crystals so far. When the size of materials shrinks into nanometer scale, not only $(0\,1\,\bar{1}\,3)$ twin, but also $(0\,1\,\bar{1}\,1)$ and $(0\,1\,\bar{1}\,2)$ twins has been observed in ZnO 1D nanostructures. The population of $(0\,1\,\bar{1}\,1)$ and $(0\,1\,\bar{1}\,2)$ twins is much lower than that of the $(0\,1\,\bar{1}\,3)$ twin, in agreement with theoretical energy calculation. Besides above three dominant twin structures, $(\bar{2}\,1\,1\,2)$ twin was also observed in 1D ZnO nanostructures.

Imaging twins by TEM prefers to carry out with incident electron beam along special orientation. The optimum orientation is parallel to the twin plan. For wurtzite structure, the beam direction is usually $[2\,\bar{1}\,\bar{1}\,0]$ and/or $[0\,1\,\bar{1}\,0]$.

Fig. 1(a) shows a typical ZnO $(0\,1\,\bar{1}\,3)$ twin structure (Ding and Wang, 2004). Its SAED pattern is displayed in Fig. 1(b), which is composed of two sets of diffraction spots that have symmetrical geometrical distribution but possibly variable intensity. The two set patterns are labeled using subscripts L and R specifying the left-hand and right-hand crystals, respectively. The common spot is the twin boundary plane $(0\,1\,\bar{1}\,3)$, as indexed in the SAED pattern, and the incident beam direction is $[\bar{2}\,1\,1\,0]$. The existence of high-density stacking faults in the dark-field image [Fig. 1(c)] indicates the large local strain. The optimum orientation to image twins is parallel to the twin plane, so that the diffraction pattern shows mirror symmetry between the two sets of diffraction spots. Fig. 1(d) is a HRTEM image recorded from the twin boundary, clearly displays the mirror symmetry between the two crystals. HRTEM image simulation was carried out to clarify the Zn arrangement at the boundary. The best-matched simulated image is inserted in Fig. 1(d). In such focus conditions identified by the simulation, the dark contrast corresponds to atom positions, mostly Zn atoms, for the contrast of O is very weak.

Normally, ZnO nanomaterials take hexagonal wurtzite structure. However, they can be cubic zinc-blende structure as well. For the atoms in both structures are tetrahedrally coordinated by atoms of the opposite species. The close-packed planes stacking in ABCABC sequence will form zinc-blende structure, while stacking in ABABAB sequence gives the wurtzite structure. The formation of $(0\,1\,\bar{1}\,3)$ twins seems relate to the zinc-blende nucleus in the growth.

It is considered that the surface contribution to the total energy becomes increasingly important as the size decreases. The favorable growth direction of 1D wurtzite nanostructures is along *c*-axis with exposed surfaces being $\{0\,1\,\bar{1}\,0\}$ or $\{2\,\bar{1}\,\bar{1}\,0\}$ (Wang et al., 2002). The *c*-axis in wurtzite structure corresponds to the $\langle 1\,1\,1\rangle$ direction in zinc-blende. The exposed surface in zinc-blende structure will be $\{1\,1\,0\}$ or $\{2\,1\,1\}$. Calculations of surface energies based on bond density reveal that the $\{0\,1\,\bar{1}\,0\}$ planes in wurtzite structure is the energetically favorable surface in 1D nanostructure system (Ding et al., 2007). This is likely a reason why ZnS nanowires take metastable wurtzite rather than stable zinc-blende (Ding et al., 2004b). However, the starting nucleus can still be in zinc-blende crystal structure for the limited high-energy surface areas. With the growth of the nucleus, the surface energy will drive the phase transition from zinc-blende to wurtzite, the eight $\langle 1\,1\,1\rangle$ directions in zinc-blende can be separated into two classes, one is cation terminated, another is anion terminated. Due to the self-catalysis effect, normally only cation terminated $\langle 1\,1\,1\rangle$ directions,

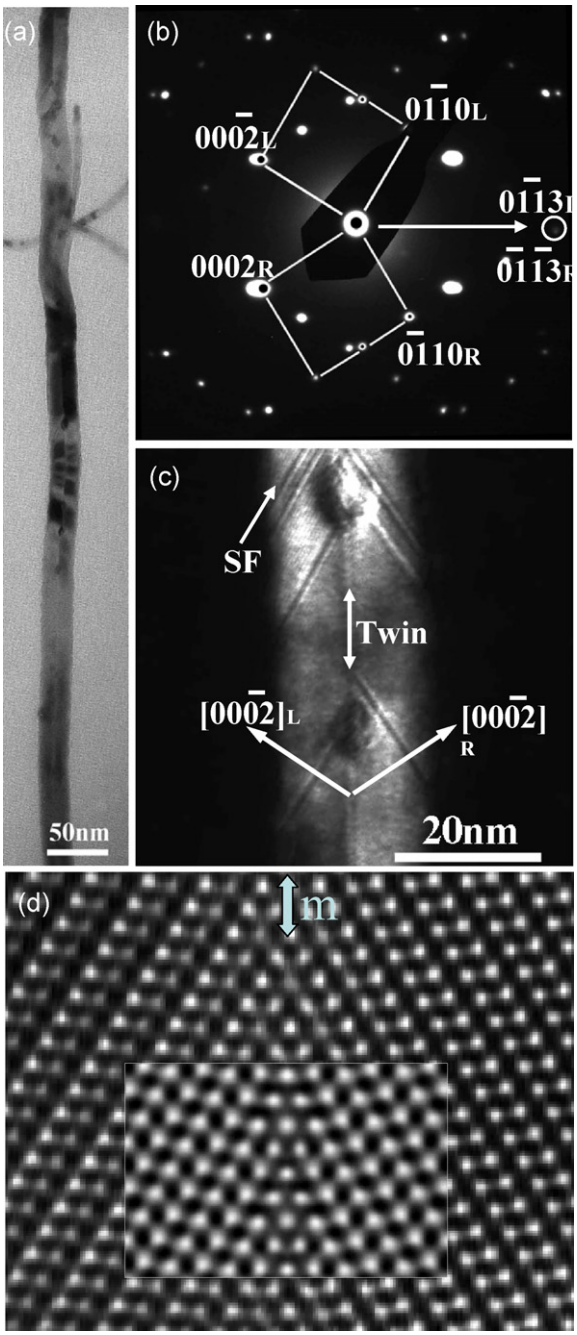

Fig. 1. (a and b) TEM image and corresponding SAED pattern of a ZnO nanobelt that has a $(0\,1\,\bar{1}\,3)$ twin parallel to the growth direction. (c) A dark-field TEM image showing the existence of stacking faults in the nanobelt. (d) HRTEM image of the $(0\,1\,\bar{1}\,3)$ twin with the incident electron beam along $[2\,\bar{1}\,\bar{1}\,0]$ direction, the simulation image is inserted (Ding and Wang, 2004).

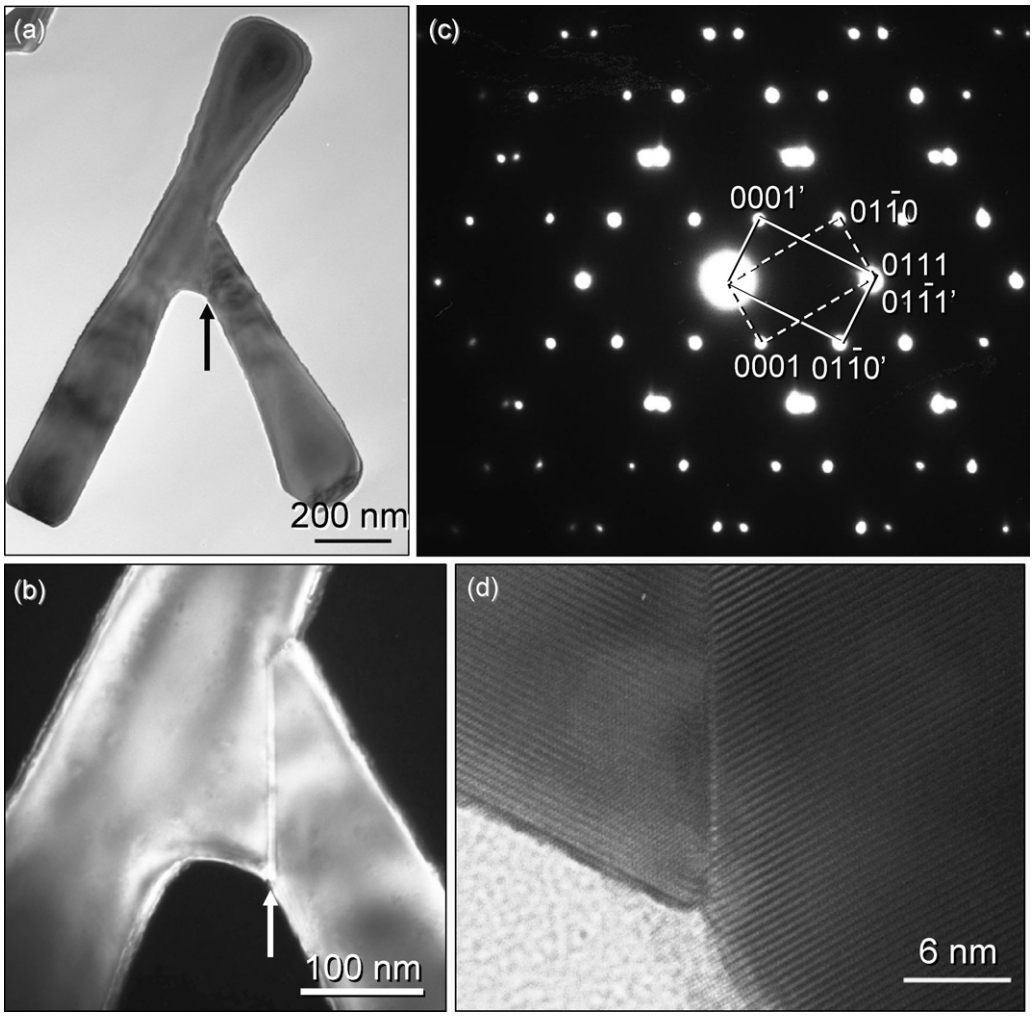

Fig. 2. (a and b) Bright-field and dark-field TEM images of a $(0\,1\,\bar{1}\,1)$ twin structure in ZnO nanobelt. (c and d) The SAED pattern and HRTEM image of the $(0\,1\,\bar{1}\,1\,0)$ twin with the incident electron beam along $[2\,\bar{1}\,\bar{1}\,0]$ direction.

corresponding to [0 0 0 1] in wurtzite, can further grow. The final structure introduced by the phase transition between zinc-blende and wurtzite is the well-known tetrapod structures (Ding et al., 2007; Fuller, 1944; Nishio et al., 1997; Ronning et al., 2005). The angle between the two cation terminated $\langle 1\,1\,1\rangle$ or [0 0 0 1] directions is around 108° in tetrapod structure, while the angles between the two [0 0 0 1] directions in the $(0\,1\,\bar{1}\,3)$ twins are 116.7° in ZnO. There are no low-index planes between the two legs of the tetrapod. However, If the legs rotate 6–9°, the conjugated plane for the $(0\,1\,\bar{1}\,3)$ twin is a favorable interface of choice. Based on above observation and discussion, we can claim that the growth of $(0\,1\,\bar{1}\,3)$ twin is possibly, related to the formation of zinc-blende nucleus.

Although $(0\,1\,\bar{1}\,1)$ and $(0\,1\,\bar{1}\,2)$ twins are not energetically favorable compared with $(0\,1\,\bar{1}\,3)$ twin, we still observed them in ZnO 1D system. The detailed synthesis process can be fund in reference (Ding et al., 2007). Fig. 2(a) and (b) give the bright-field and dark-field TEM images of a $(0\,1\,\bar{1}\,1)$ twin. The twin plane has been highlighted by an arrowhead. The SAED pattern is displayed in Fig. 2(c). Solid and dashed rectangles separate the two set of diffraction spots. The shared plane can be identified as $(0\,1\,\bar{1}\,1)$, corresponding to the formation of $(0\,1\,\bar{1}\,1)$ twin structure. The HRTEM image in Fig. 2(d) gives clear mirror symmetry between the two parts of the twin.

The dark-field image and SAED pattern of a $(0\,1\,\bar{1}\,2)$ twin is displayed in Fig. 3(a) and (b), respectively. The diffraction pattern unambiguously indicates the existence of a $(0\,1\,\bar{1}\,2)$ twin by the shared $(0\,1\,\bar{1}\,2)$ diffraction of the two set of diffraction spots. Besides the diffraction spots coming from the twin, there still have extra diffraction spots in weak intensity, they are from double diffraction. Based on the image in Fig. 3(a), we cannot image a smooth interface between the two parts of the twined crystals. This may indicate the energy of $(0\,1\,\bar{1}\,2)$ twin is high.

Besides $(0\,1\,\bar{1}\,3)$, $(0\,1\,\bar{1}\,2)$ and $(0\,1\,\bar{1}\,1)$ twin structures, we also found the $(\bar{2}\,1\,1\,2)$ twin structure in ZnO nanobelts (Ding and Wang, 2004). Fig. 4(a) and (b) are bright-field and dark-field images of the ZnO twined nanobelt. The SAED pattern in Fig. 4(c) indicates that the mirror plane of the twin structure is a $(\bar{2}\,1\,1\,2)$ plane. Only (0 0 0 2) fringes can be observed in the HRTEM image, due to the inter-plane distance of $(\bar{2}\,1\,1\,0)$ being smaller than the resolution of the microscope. The diffraction contrast in Fig. 4(a) and (b) indicates the large stain in the belt. Formation of stacking faults is an effective way to release the strain. However, along such incident beam direction, the contrast of staking faults should be extinguished.

3.2. Staking faults

Stacking faults are the most frequently observed planar defects in 1D ZnO nanostructures. They are formed by the changes in

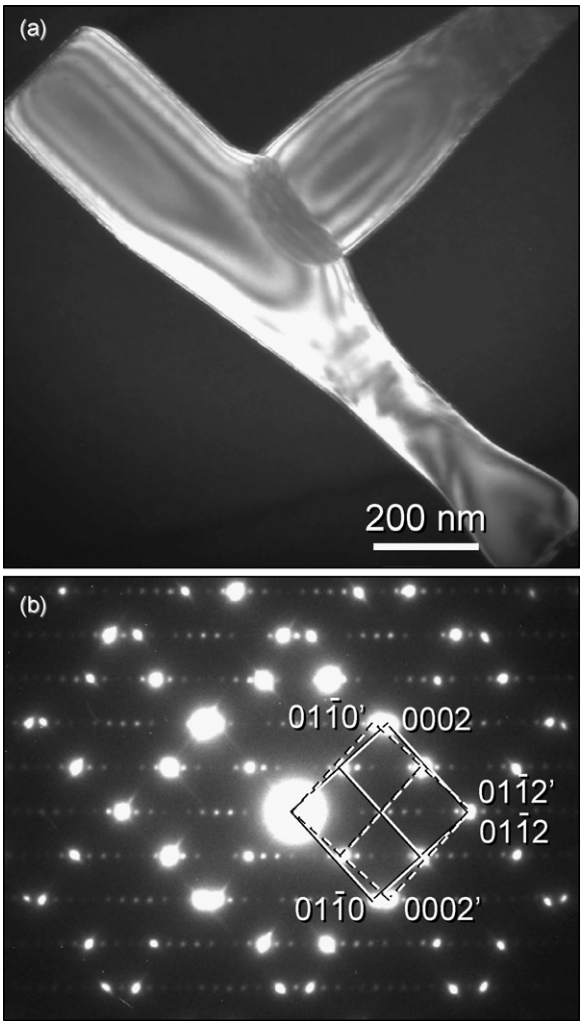

Fig. 3. (a) Dark-field image of a (0 1 $\bar{1}$ 2) twin in ZnO nanobelt, its SAED pattern is displayed in (b).

stacking sequence of close-packed planes. Depending on the stacking faults lying in or perpendicular to their closed-packed plane, they are named basal-plane and prismatic-plane stacking faults, separately.

In the wurtzite structure, there are three possible types of basal-plane stacking faults, I_1, I_2, and E in bulk materials, which are produced by extracting one or two periodic layers, and inserting a layer, respectively (Potin et al., 2000; Stampfl and Van de Walle, 1998). The nature of stacking faults can be identified by combining HRTEM with image simulation or diffraction contrast extinguishing conditions. For imaging the contrast of stacking faults, the diffraction beam **g** has to avoid the extinguishing condition as **g**·**R** = 0, or *n* where **R** is the displacement crossing the defect and *n* is an integer. As we know, the **R** of stacking faults in wurtzite structures are 1/3[0 1 $\bar{1}$ 0] + 1/2[0001] for type I_1 case and 2/3[0 1 $\bar{1}$ 0] fro type I_2 case.

A stacking fault in a ZnO nanobelt is displayed in Fig. 5(a). Its HRTEM image is recorded in Fig. 5(b). The synthesis process of the ZnO nanobelts are the same as that reported by Pan et al. (2001). An arrowhead highlights the *c* direction in the image. In spite of the perfect stacking sequence of wurtzite structure as ABABAB along the [0 0 0 1] direction, a new consequence as identified as ...ABABACAC... in the defect area suggests the existence of an I_1 stacking fault. The displacement across the I_1 basal-plane stacking fault can be identified as **R** = 1/3[0 1 $\bar{1}$ 0] + 1/2 [0 0 0 $\bar{1}$] = 1/6[0 2 $\bar{2}$ $\bar{3}$].

Fig. 6(a) is a low magnification TEM image of another ZnO [0 1 $\bar{1}$ 0] growth nanobelt. There are two different basal-plane stacking faults exist in Fig. 6(a), the top one is the I_1 stacking fault discussed in Fig. 5. A HRTEM image of the bottom defect is shown in Fig. 6(b). In the defect area, the stacking sequence can be described as ...ABABCACAC... It can be classified as an intrinsic type I_2 basal-plane stacking fault since it is equivalent to extracting two periodic layers and a 2/3[0 1 $\bar{1}$ 0] translation displacement has been measured across the defect.

From crystal structural point of view, hexagonal wurtzite structure takes space group as $P6_3mc$. It can be described as a number of alternating planes composed of tetrahedrally coordinated cations and anions, stacking alternatively along the *c*-axis (Dulub et al., 2003). The oppositely charged ions produce positively charged (0 0 0 1) and negatively charged (0 0 0 $\bar{1}$) polar surfaces, resulting in a normal dipole moment and sometimes even spontaneous polarization along the *c*-axis as well as a divergence in surface energy. For a general case, one-dimensional wurtzite nanostructures usually grow along the *c*-axis and their side surfaces are {0 1 $\bar{1}$ 0} and/or {2 $\bar{1}$ $\bar{1}$ 0} due to their lower energies than that of (0 0 0 1), resulting in almost neutralized dipole moment. I_1 type of basal-plane stacking faults can be easily formed

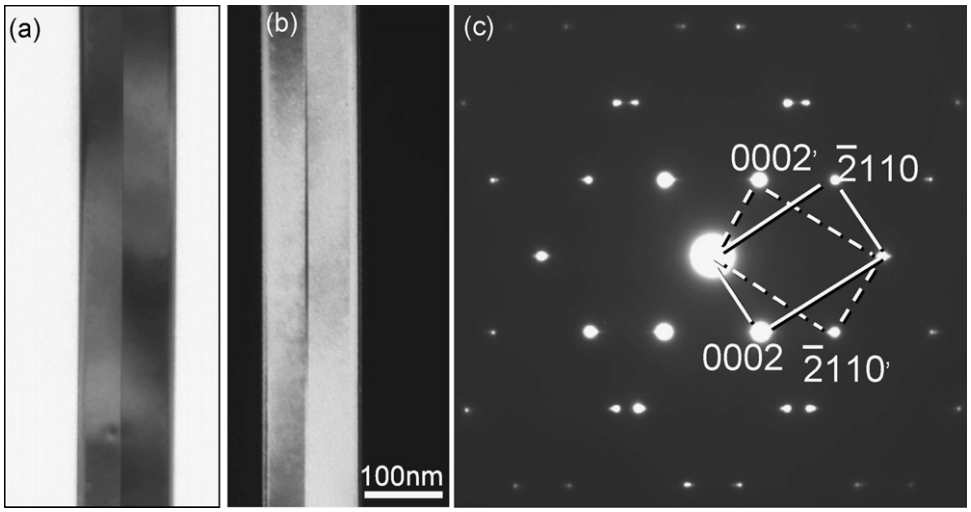

Fig. 4. Bright-field (a) and dark-field (b) TEM images of a ($\bar{2}$ 1 1 2) twined ZnO nanobelt. (c) The SAED pattern with the incidence electron beam along [0 1 $\bar{1}$ 0] direction (Ding and Wang, 2004).

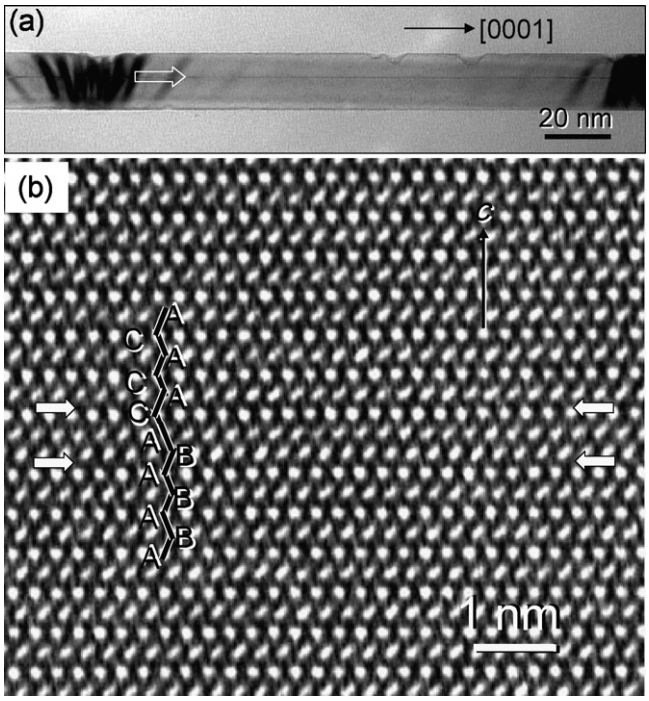

Fig. 5. Low-magnification (a) and HRTEM (b) image in ZnO nanobelt showing the type I_1 intrinsic basal-plane stacking fault. The incident electron beam in the HRTEM image is along [2 $\bar{1}$ $\bar{1}$ 0] direction.

in those [0 0 0 1] growth nanowires. The 1D nanostructures growing normal to the [0 0 0 1] direction, as the cases shown in Figs. 5 and 6, are normally accompanied by at least a stacking fault from the beginning to end. Noticing the surface kink at the intersection between the stacking fault and the growth front, it can be a preferred position to adsorb the vapor molecules to accelerate the growth along such direction. As a result, the existence of basal-plane stacking faults can span the energy barrier set by the polar surfaces, and then lead the 1D nanostructures to grow along [0 1 $\bar{1}$ 0] direction.

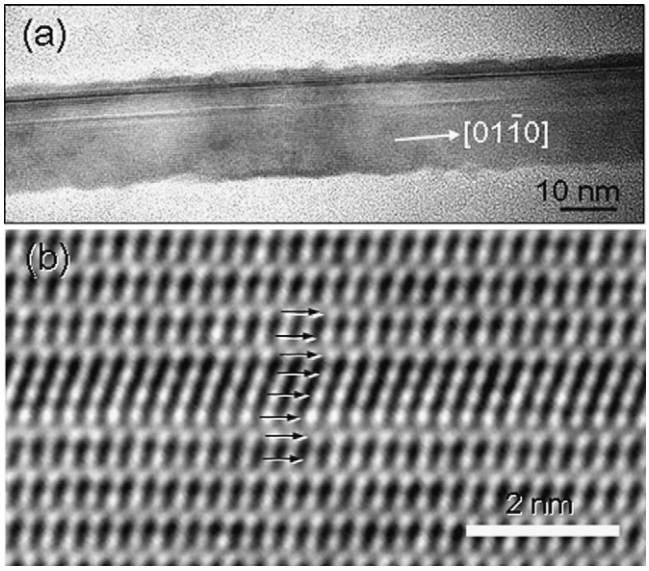

Fig. 6. Low-magnification (a) and HRTEM (b) images of a [0 1 $\bar{1}$ 0] growth ZnO nanobelt with incident electron beam along [2 $\bar{1}$ $\bar{1}$ 0] direction. The defect in (b) belongs to the type I_2 stacking fault.

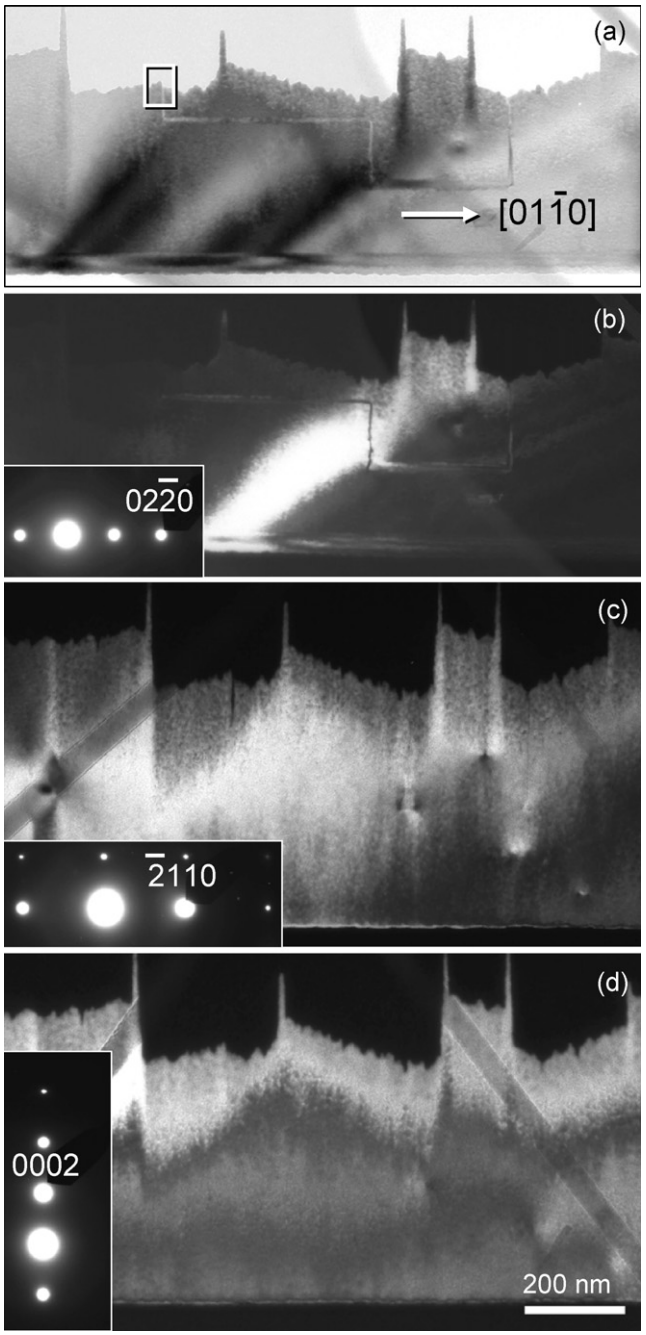

Fig. 7. Bright-field (a) and dark-field (b) images of a [0 1 $\bar{1}$ 0] growth ZnO nanobelt recorded under two-beam condition with $g = (0\,2\,\bar{2}\,0)$. Prismatic and basal-plane stacking faults coexist in the belt. In the dark-field images recorded using $g = (\bar{2}\,1\,1\,0)$ (c) and 0 0 0 2 (d), the contrast of the defect vanishes.

Besides basal-plane stacking faults, we also observed prismatic-plane stacking faults in wider ZnO nanobelts (~1 μm). Prismatic-plane stacking faults have two configurations classified by the displacements across them. The displacements across the defect, one is 1/2 ⟨0 1 $\bar{1}$ $\bar{1}$⟩, and another is 1/6 ⟨0 2 $\bar{2}$ $\bar{3}$⟩ (Vermaut et al., 1999; Northrup, 1998). In order to determine the structural nature of the defect in the nanobelts, a series of dark-field images have been recorded as shown in Fig. 7. The defect contrast can be seen clearly in Fig. 7(a) and (b), which are the corresponding bright-field and dark-field images under two-beam condition with the $g = (0\,2\,\bar{2}\,0)$. The diffraction condition is inserted in Fig. 7(b). After identifying the [0 1 $\bar{1}$ 0] direction by the diffraction pattern, we

know that part of the defect lies in the basal plane, part in prismatic plane. The extended contrast of defects while titling the belt suggests that they are planar defects and rules out the possibility of dislocation loops. Only one set of SAED pattern was recorded from the defects area, thus they cannot be twin structures. They must be stacking faults, part in basal plane, and part in prismatic plane. By further tilting the nanobelt, we get two extinguishing conditions of the defects as shown in Fig. 7(c) and (d). They correspond to diffraction g of $(\bar{2}\,1\,1\,0)$ and $(0\,0\,0\,2)$, respectively. Both displacements $1/2\langle 0\,1\,\bar{1}\,\bar{1}\rangle$ and $1/6\langle 0\,2\,\bar{2}\,\bar{3}\rangle$ can be perpendicular to $(\bar{2}\,1\,1\,0)$, or an integer when multiplied with $(0\,0\,0\,2)$. However, if the displacement is $1/2\langle 0\,1\,\bar{1}\,\bar{1}\rangle$, the stacking faults may lose contrast in the dark-field image formed by the $(0\,2\,\bar{2}\,0)$ diffraction. As a conclusion, the stacking faults should take the displacement of $1/6\langle 0\,2\,\bar{2}\,\bar{3}\rangle$, which are the same as that of I_1 basal-plane stacking fault. HRTEM study in Fig. 8 further confirmed our deduction. The HRTEM images from the basal plane part of the defects are the same as that of I_1 stacking fault shown in Fig. 5(b).

Fig. 8(a) is a HRTEM image recorded from the prismatic plane part of the defect shown in Fig. 7(a). Fig. 8(b) gives a magnified defect area in (a). The displacement along the c-axis can be easily identified. The projected width of the I_1 basal-plane stacking fault along $[2\,\bar{1}\,\bar{1}\,0]$ direction is just an atomic plane thickness as shown in Fig. 5. However, the projection of the prismatic-plane stacking fault in the same direction is nearly 3 nm in Fig. 8(b). A possible explanation is that the defect is not edgy-on in Fig. 8. The prismatic stacking fault most likely lies in $(\bar{2}\,1\,1\,0)$ plane instead of the $(0\,1\,\bar{1}\,0)$ plane. There is a $1/3[0\,1\,\bar{1}\,0] + 1/2[0\,0\,0\,\bar{1}] = 1/6\langle 2\,0\,2\,\bar{3}\rangle$ translation across the defect, which is self-consistent with the result received from diffraction contrast analysis presented above.

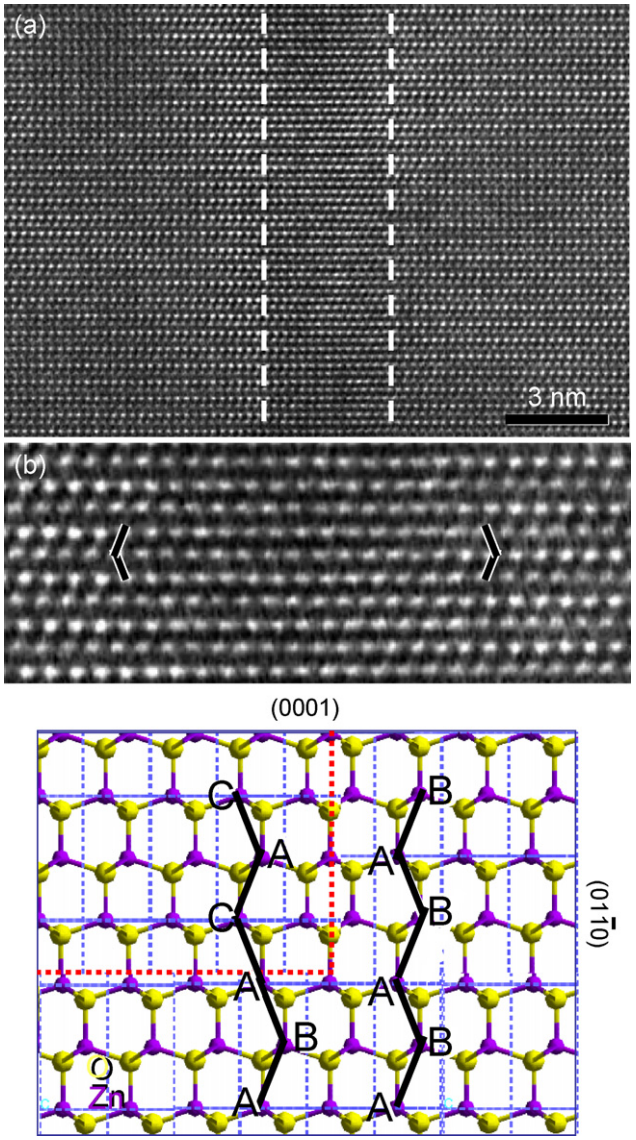

Fig. 8. (a) and (b) HRTEM images of ZnO nanobelts with incident electron beam along $[2\,\bar{1}\,\bar{1}\,0]$ direction, showing the prismatic-plane stacking fault. Atomic model (c) shows the stacking fault folding from basal to prismatic plane.

In order to emphasize the difference between the basal-plane stacking fault and prismatic-plane one, an atomic model was built as shown in Fig. 8(c). The horizontal red lines localized the basal-plane stacking fault, while the vertical red line gives the prismatic-plane stacking fault. The displacement between the left-up red line circled part and others is $1/6\langle 2\,0\,2\,\bar{3}\rangle$. The ideal stacking sequences of Zn and oxygen ions can be described as . . .AaBbAaBbAaBb. . ., the capital and lower-case letters give the stacking sequences of zinc and oxygen ions in $[0\,0\,0\,1]$ direction, respectively. For simplicity, we only consider the stacking sequence of zinc ions as ABABAB. . .in this work, while the sequences of oxygen ions are the same. When the defect remains in the basal plane, compared with perfect crystal case, the closest neighbors of an ion at defect area do not change and the bonding length between cations and anions remains the same. The only change occurs at the second closest neighbors, which is shifted from a hexagonal close-packed (hcp) system to a face center cubic (fcc) system. However, when the defect folds from basal plane to prismatic plane, if the defect located in a $(0\,1\,\bar{1}\,0)$ plane, then, at the vertical red line located area, some of the bonds are compressed, some are expanded. The final configuration is the system energy will increase. This is why the prismatic-plane stacking fault chooses $\{2\,\bar{1}\,\bar{1}\,0\}$ planes.

The formation of the prismatic-plane stacking faults seems be related to the secondary growth led by the self-catalysis effect. We can find basal-plane stacking faults in the bottom side of the nanobelt in Fig. 7 and they cross the whole nanobelt from the beginning to end, and are presumed to guide the dominant growth of the nanobelt along $[0\,1\,\bar{1}\,0]$. The exposed top and low surfaces of the nanobelt then are Zn-terminated (0001) and oxygen terminated $(0\,0\,0\,\bar{1})$ plane, respectively. The self-catalysis growth at the Zn-terminated surface will lead the secondary growth at $(0\,0\,0\,1)$ surface, which is the up top of the nanobelt in Fig. 8. The domains growing from different nucleuses at $(0\,0\,0\,1)$ surface will merge together at the end, however, the stacking faults nucleated in each domain are hard to cross the boundary to elongate into nearby domain, further, the defect properties require that they cannot be terminated inside the body, therefore, in order to minimize the system energy, the defects lying in the domain boundaries, here those prismatic planes, will be favorable. It corresponds to fold the stacking faults from basal plane to prismatic plane, and then we can observe those prismatic-plane stacking faults.

3.3. Inversion domain walls

Planar defects, such as basal-plane stacking faults, can guide ZnO nanobelts growing along $[0\,1\,\bar{1}\,0]$ direction to expose the polar surface as side surfaces. Inversion domain walls form in ZnO as a result of doping (Yan et al., 1998; McCoy et al., 1997; Cannard and Tilley, 1988; Li et al., 2000). The doped impurity chosen was indium. As a result, the $[0\,1\,\bar{1}\,0]$ growth nanobelts were formed (Kong and Wang, 2003; Kong et al., 2004; Ding et al., 2004a). Because the nanobelts have large exposed polar surfaces, they can self-coil to form nanospring or nanorings.

Fig. 9(a) shows a ZnO nanobelt with inversion domain walls parallel to the $(0\,0\,0\,1)$ polar surfaces. X-ray energy-dispersive

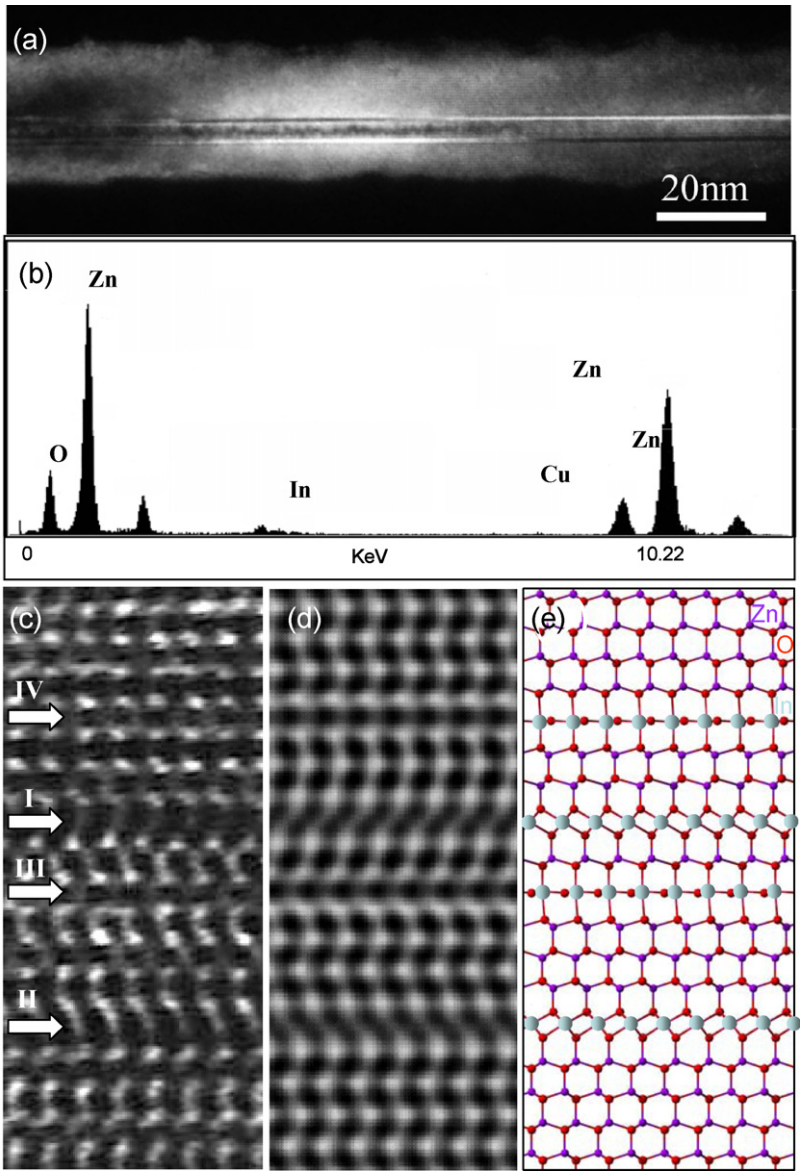

Fig. 9. (a) Dark-field TEM image of ZnO nanobelt with inversion domain boundaries. (b) EDS spectrum showing the presence of In ions in the structure. Experimental (c) and simulated (d) HRTEM images of the inversion domain boundaries with incident electron beam along [2 $\bar{1}$ $\bar{1}$ 0] direction. (e) The structural model used in the simulation. The simulation is for a sample thickness of 2.924 nm, defocus −28.67 nm, for JEOL 4000EX at 400 kV (Ding et al., 2004a).

spectrum (EDS) required from the nanobelt shows the presence of minor indium besides majority of Zn and O (Cu and Si signals come from copper grid and the substrate) [Fig. 9(b)]. Quantitative analysis indicates the atomic ratio of In:Zn ≈ 1:15, suggesting that indium ions are successfully doped in the ZnO lattice. The HRTEM image in Fig. 9(c) presents a nanobelt with two sharp-contrast plane defects. After constructing several possible structural models, we did the detailed image simulations in reference to the experimental data. If we consider the two dark layers (labeled **I** and **II** in the image) as two In–O octahedral layers, we found the best-matched structural model is the one displayed in Fig. 9(e). If we define the (0 0 0 1) surface is Zn-terminated and the (0 0 0 $\bar{1}$) surface is oxygen-terminated, so that the polarization is along *c*-axis, the two slabs of ZnO on both sides of the In–O octahedral layer must have opposite polarization, which means that the In–O layer effectively induces a "head-to-head" polarization domain, so called inversion domain boundary. To configure the two sharply contrasted plane defects (**I** and **II**), there must exist another type of defect (labeled as **III**) between **I** and **II** layers, and it should correspond to a "tail-to-tail" inversion domain wall. The **III** layer does exit in the image and the bright spots at its very adjacent forms a rectangle pattern. On the other hand, based on the structural model of In_2O_3, the two slabs of ZnO on either sides of In–O octahedral layer can take not only head-to-head polarity, but also tail-to-tail polarity as presented in Fig. 9(e). In the first case, the fourfold symmetry axis of the In–O octahedra lies in the ZnO *c*-plane to form a head-to-head inversion domain wall. In the second case, the fourfold symmetry axis of the In–O octahedron is parallel to the **c**-axis to form a tail-to-tail inversion domain wall. Such tail-to-tail layer also exists above **I** layer, as labeled to be **IV** layer. The transverse translation of the **IV** layer may be resulted from the relocation of the doped indium ions. It is noteworthy that the translation in the [0 0 0 1] direction across the tail-to-tail IDB is very small, and there is no translation along the [0 1 $\bar{1}$ 0] direction. A simulated image based on the model in Fig. 9(e) is shown in Fig. 9(d). An excellent match between the simulated and the experimental images supports our model.

4. Conclusion

By using transmission electron microscopy, three different types of planar defects in 1D ZnO nanostructures have been characterized. They are $(0\,1\,\bar{1}\,1)$, $(0\,1\,\bar{1}\,2)$, $(0\,1\,\bar{1}\,3)$ and $(\bar{2}\,1\,1\,2)$ twins, I_1, I_2 basal-plane stacking faults and $1/6\langle 2\,0\,2\,\bar{3}\rangle$ prismatic-plane stacking faults, and inversion domain walls as a result of impurity doping. The formation mechanism of each type of planar defect was discussed. The fast growth of special orientation guided by planar defects has been emphasized. This study provides a systematic analysis of planar defects that are frequently observed in 1D ZnO nanostructures.

Acknowledgements

The research was supported by NSF, DARPA, NASA and BES DOE. Thanks Dr. Rusen Yang, and Dr. X.Y. Kong for providing the samples.

References

Arnold, M.S., Avouris, P., Pan, Z.W., Wang, Z.L., 2003. Field-effect transistors based on single semiconducting oxide nanobelts. J. Phys. Chem. B 107, 659–663.

Bai, X.D., Gao, P.X., Wang, Z.L., Wang, E.G., 2003. Dual-mode mechanical resonance of individual ZnO nanobelts. Appl. Phys. Lett. 82, 4806–4808.

Bere, A., Serra, A., 2003. Atomic structures of twin boundaries in GaN. Phys. Rev. B 68, 033305.

Cannard, P.J., Tilley, R.J.D., 1988. New intergrowth phases in the Zno–In_2O_3 System. J. Solid State Chem. 73, 418–426.

Comini, E., Faglia, G., Sberveglieri, G., Pan, Z.W., Wang, Z.L., 2002. Stable and highly sensitive gas sensors based on semiconducting oxide nanobelts. Appl. Phys. Lett. 81, 1869–1871.

Ding, Y., Kong, X.Y., Wang, Z.L., 2004a. Doping and planar defects in the formation of single-crystal ZnO nanorings. Phys. Rev. B 70, 235408.

Ding, Y., Wang, X.D., Wang, Z.L., 2004b. Phase controlled synthesis of ZnS nanobelts: zinc blende vs wurtzite. Chem. Phys. Lett. 398, 32–36.

Ding, Y., Wang, Z.L., 2004. Structure analysis of nanowires and nanobelts by transmission electron microscopy. J. Phys. Chem. B 108, 12280–12291.

Ding, Y., Wang, Z.L., Sun, T.J., Qiu, J.S., 2007. Zinc-blende ZnO and its role in nucleating wurtzite tetrapods and twinned nanowires. Appl. Phys. Lett. 90, 153510.

Dulub, O., Diebold, U., Kresse, G., 2003. Novel stabilization mechanism on polar surfaces: ZnO(0001)–Zn. Phys. Rev. Lett. 90, 016102.

Fuller, M.L., 1944. Twinning in zinc oxide. J. Appl. Phys. 15, 164–170.

Hughes, W.L., Wang, Z.L., 2003. Nanobelts as nanocantilevers. Appl. Phys. Lett. 82, 2886–2888.

Kong, X.Y., Ding, Y., Yang, R., Wang, Z.L., 2004. Single-crystal nanorings formed by epitaxial self-coiling of polar nanobelts. Science 303, 1348–1351.

Kong, X.Y., Wang, Z.L., 2003. Spontaneous polarization-induced nanohelixes, nanosprings, and nanorings of piezoelectric nanobelts. Nano Lett. 3, 1625–1631.

Li, C., Bando, Y., Nakamura, M., Kimizuka, N., 2000. Relation between In ion ordering and crystal structure variation in homologous compounds $InMO_3(ZnO)(m)$ (M = Al and In; m = integer). Micron 31, 543–550.

McCoy, M.A., Grimes, R.W., Lee, W.E., 1997. Planar intergrowth structures in the ZnO–In_2O_3 system. Philos. Mag. A 76, 1187–1201.

Nishio, K., Isshiki, T., Kitano, M., Shiojiri, M., 1997. Structure and growth mechanism of tetrapod-like ZnO particles. Philos. Mag. A 76, 889–904.

Northrup, J.E., 1998. Theory of the (1(2)under-bar-10) prismatic stacking fault in GaN. Appl. Phys. Lett. 72, 2316–2318.

Pan, Z.W., Dai, Z.R., Wang, Z.L., 2001. Nanobelts of semiconducting oxides. Science 291, 1947–1949.

Potin, V., Ruterana, P., Nouet, G., 2000. HREM study of stacking faults in GaN layers grown over sapphire substrate. J. Phys-Condens. Matter 12, 10301–10306.

Ronning, C., Shang, N.G., Gerhards, I., Hofsass, H., Seibt, M., 2005. Nucleation mechanism of the seed of tetrapod ZnO nanostructures. J. Appl. Phys. 98, 034307.

Sauer, G., Brehm, G., Schneider, S., Nielsch, K., Wehrspohn, R.B., Choi, J., Hofmeister, H., Gosele, U., 2002. Highly ordered monocrystalline silver nanowire arrays. J. Appl. Phys. 91, 3243–3247.

Shi, L., Hao, Q., Yu, C.H., Mingo, N., Kong, X.Y., Wang, Z.L., 2004. Thermal conductivities of individual tin dioxide nanobelts. Appl. Phys. Lett. 84, 2638–2640.

Stampfl, C., Van de Walle, C.G., 1998. Energetics and electronic structure of stacking faults in AlN, GaN, and InN. Phys. Rev. B 57, R15052–R15055.

Vermaut, P., Nouet, G., Ruterana, P., 1999. Observation of two atomic configurations for the {1(2)over-bar-10} stacking fault in wurtzite (Ga, Al) nitrides. Appl. Phys. Lett. 74, 694–696.

Wang, Z.L., 2003a. Nanowires and Nanobelts, vol. I. Metal and Semiconductor, Nanowires. Kluwer Academic Publisher, New York.

Wang, Z.L., 2003b. Nanowires and Nanobelts, vol. II. Nanowires and Nanobelts of Functional Materials. Kluwer Academic Publisher, New York.

Wang, Z.L., Pan, Z.W., Dai, Z.R., 2002. Structures of oxide nanobelts and nanowires. Microsc. Microanal. 8, 467–474.

Wiley, B.J., Xiong, Y.J., Li, Z.Y., Yin, Y.D., Xia, Y.A., 2006. Right bipyramids of silver: a new shape derived from single twinned seeds. Nano Lett. 6, 765–768.

Yan, Y., Pennycook, S.J., Dai, J., Chang, R.P.H., Wang, A., Marks, T.J., 1998. Polytypoid structures in annealed In_2O_3–ZnO films. Appl. Phys. Lett. 73, 2585–2587.